



Article

Enhancement in Thermal Energy and Solute Particles Using Hybrid Nanoparticles by Engaging Activation Energy and Chemical Reaction over a Parabolic Surface via Finite Element Approach

Yu-Ming Chu ^{1,2}, Umar Nazir ³, Muhammad Sohail ^{3,*} , Mahmoud M. Selim ^{4,5} and Jung-Rye Lee ^{6,*}¹ Institute for Advanced Study Honoring Chen Jian Gong, Hangzhou Normal University, Hangzhou 311121, China; chuyuming@zjhu.edu.cn² Department of Mathematics, Huzhou University, Huzhou 313000, China³ Department of Applied Mathematics and Statistics, Institute of Space Technology, P.O. Box 2750, Islamabad 44000, Pakistan; nazir_u2563@yahoo.com⁴ Department of Mathematics, Al-Aflaj College of Science and Humanities Studies, Prince Sattam Bin Abdulaziz University, Al-Aflaj 710-11912, Saudi Arabia; m.selim@psau.edu.sa⁵ Department of Mathematics, Suez Faculty of Science, Suez University, Suez 34891, Egypt⁶ Department of Data Science, Daejin University, Pocheon-si 11159, Korea

* Correspondence: muhammad_sohail111@yahoo.com (M.S.); jrlee@daejin.ac.kr (J.-R.L.)



Citation: Chu, Y.-M.; Nazir, U.; Sohail, M.; Selim, M.M.; Lee, J.-R. Enhancement in Thermal Energy and Solute Particles Using Hybrid Nanoparticles by Engaging Activation Energy and Chemical Reaction over a Parabolic Surface via Finite Element Approach. *Fractal Fract.* **2021**, *5*, 119. <https://doi.org/10.3390/fractalfract5030119>

Academic Editors: Lanre Akinyemi, Mostafa M. A. Khater, Mehmet Senol and Hadi Rezazadeh

Received: 15 August 2021

Accepted: 10 September 2021

Published: 13 September 2021

Publisher's Note: MDPI stays neutral with regard to jurisdictional claims in published maps and institutional affiliations.



Copyright: © 2021 by the authors. Licensee MDPI, Basel, Switzerland. This article is an open access article distributed under the terms and conditions of the Creative Commons Attribution (CC BY) license (<https://creativecommons.org/licenses/by/4.0/>).

Abstract: Several mechanisms in industrial use have significant applications in thermal transportation. The inclusion of hybrid nanoparticles in different mixtures has been studied extensively by researchers due to their wide applications. This report discusses the flow of Powell–Eyring fluid mixed with hybrid nanoparticles over a melting parabolic stretched surface. Flow rheology expressions have been derived under boundary layer theory. Afterwards, similarity transformation has been applied to convert PDEs into associated ODEs. These transformed ODEs have been solved the using finite element procedure (FEP) in the symbolic computational package MAPLE 18.0. The applicability and effectiveness of FEM are presented by addressing grid independent analysis. The reliability of FEM is presented by computing the surface drag force and heat transportation coefficient. The used methodology is highly effective and it can be easily implemented in MAPLE 18.0 for other highly nonlinear problems. It is observed that the thermal profile varies directly with the magnetic parameter, and the opposite trend is recorded for the Prandtl number.

Keywords: mathematical modeling; ordinary and partial differential equations; parametric investigation; finite element technique; grid independent investigation; thermal enhancement

1. Introduction

Due to rapid developments, the modeling of real phenomena is a hot topic of research due to its numerous applications and physical significance. Engineers, physicists and modeling experts have proposed and developed different relations by seeing the materials characteristics. Eyring–Powell is an important material whose constitute relation is

$$\tau^* = \mu^* \nabla V + \frac{1}{\gamma^*} \sinh^{-1} \left(\frac{\nabla V}{C^*} \right), \left| \left(\frac{\nabla V}{C^*} \right) \right| \ll 1.$$

Several important studies on this model have been reported. For instance, Islam et al. [1] studied Powell–Eyring fluid over an inclined slider. They used the lubricant approach to derive a constitutive equation for the considered phenomenon. They used the homotopy perturbation scheme (HPS) to compute the solution. The impacts of numerous involved parameters on the velocity field are sketched out, and their behavior is explained via the underlying physics principles. Patel and Timol [2] computed the numerical solution

of the Powell–Eyring model after reducing the boundary layer PDEs into ODEs. Several important graphs have been plotted to monitor the bearings of different emerging parameters. The homotopy analysis approach (HAA) has been employed by Khan et al. [3] to discuss the movement of the Powell–Eyring material over a rotating disc. They described the convergence region/domain of the considered problem by sketching the h-curves. They recorded a decline in the velocity field against the fluid parameter in both axial and tangential directions. Moreover, the opposite trend in velocity was recorded for Reynolds number. Hayat et al. [4] worked on the convective axisymmetric flow of the Powell–Eyring model via the optimal homotopic approach. They showed the effectiveness of this methodology by tabulating the error analysis and CPU time. Moreover, the authenticity of the obtained results was confirmed by comparing the obtained results with those available in the open literature. They found a depreciation in the thermal field against the fluid parameter, and an escalation was observed with Biot number. Krishna et al. [5] computed a dual solution for an unsteady Powell–Eyring model in the presence of thermal radiation. They further elaborated their results for suction and injection cases. They recorded enhancements in the mass and heat transfer rates against the fluid parameter, whereas augmentations in the unsteadiness parameter reduce the skin friction coefficient. Kumar et al. [6] examined the flow of a magneto Powell–Eyring model in an annulus. They solved the modeled problem via the ND-Solve tool in the MATHEMATICA 12.0 symbolic package.

The exploration of thermal transportation in fluid flows is an attractive topic for researchers due to its wide applications. Moreover, thermal stability/instability is in high demand in the current era. Buongiorno proposed the relation in nanofluids by incorporating Brownian diffusion and thermophoresis [7,8]. Several other relations are available in the open literature, discussing the contributions of shape factors and nanoparticles [9–11] mixed in the base fluids, which is beneficial for the enhancement of thermal transportation. For instance, Khanafer and Vafai [12] reported a critical analysis on viscosity and thermal conductivity, which were introduced and synthesized by them. They stated that at a low volume fraction, a correlation can be established for effective thermal conductivity. In their survey, they presented different empirical relations for heat capacitance, the thermal expansion coefficient and the effective viscosity. Saba et al. [13] worked on radiative boundary layer flow in a curved configuration conveying CNTs particles. The modeling of thermal transport is presented with internal heating aspects. They tackled the modeled problem via a shooting approach by using the MATHEMATICA computational package. They presented a comparative analysis for the validity and authenticity of the obtained results. They recorded a decline in the thermal profile by enhancing the heat absorption parameter, and an upsurge was recorded against the heat generation parameter. Qasim et al. [14] utilized Buongiorno's model to investigate thermal and mass transportation in a thin-film MHD flow model under dissipation via the shooting approach. They monitored the enhancement in the mass and heat transportation coefficients against the unsteadiness parameter. Awais et al. [15] examined the involvement of slips in MHD stretched stagnation point nanofluids via an analytical approach. They plotted the slippage contribution via streamlines plots. They showed that 15th order approximations are sufficient for the convergent solution of velocity distribution and concentration, and thermal distributions required 25th approximations for their convergent solutions. Moreover, enhancements have been observed in temperature against the thermophoresis parameter. Some novel contributions regarding transport problems are covered in [16–19].

The above-listed contributions do not show the use of the Powell–Eyring model over a stretched parabolic surface in the presence of activation energy, Joule heating and MHD effect. So far, no such attempt has been noted. This contribution will be used as a reference to further study thermal and mass transportation over a parabolic stretched surface with several important aspects. The reported study is arranged in the following fashion: Section 1 contains a literature survey; modeling is included in Section 2; a novel numerical tool to handle the coupled nonlinear ODEs is listed in Section 3; Section 4

contains the description of obtained results and the important results are listed in Section 5. The view of hybrid nanoparticles and nanoparticles in base fluids is shown in Figure 1.

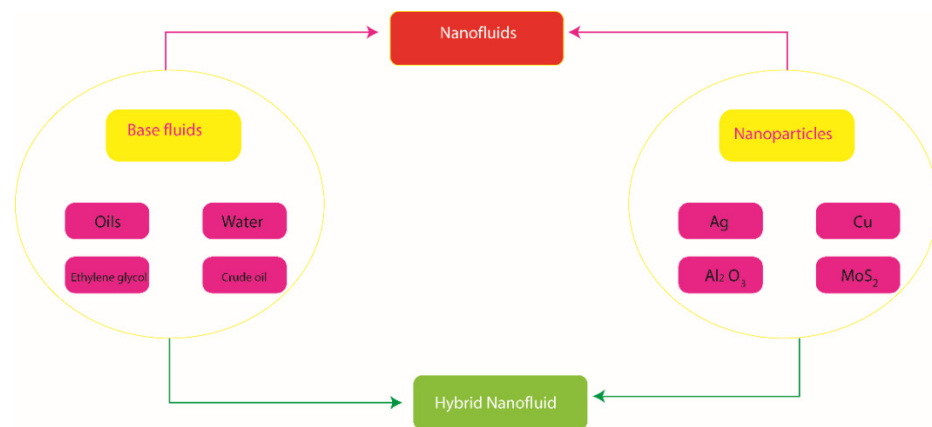


Figure 1. The view of hybrid nanoparticles and nanoparticles in base fluids.

2. Formulation of Physical Model

The physical aspects of thermal energy and solute particles in the rheology of Eyring–Powell liquid are addressed for its passage over a parabolic heated surface. The enhancements in solute and heated particles are analyzed using the concepts of hybrid nanoparticles and nanoparticles. A layer of fluid particles is generated due to the movement of the wall, which accelerates with velocity $\tilde{U}_w = a(b+x)^m$. The mathematical model is developed using the following assumptions:

- Two dimensional flow phenomenon;
 - The magnetic field is considered normally aligned to the heated surface;
 - The theory of Soret and Dufour influences is used in energy and concentration equations;
 - The roles of heat generation and chemical species are considered;
 - The activation energy is addressed in solute particles;
 - Eyring–Powell liquid is suspended along with hybrid nanoparticles and nanoparticles;
 - The base fluid is assumed to be ethylene glycol;
 - The role of bio-convection phenomena is excluded.
- Various shapes of nanoparticles (cylinder, platelet and sphere) are visualized.

The current model with the considered effects is captured by Figure 2. It can be noticed that the magnetic field is assumed to move in the y -direction, whereas the x -axis moves in the horizontal direction. Moreover, illustration of various shapes related to nanoparticles is shown in Figure 3.

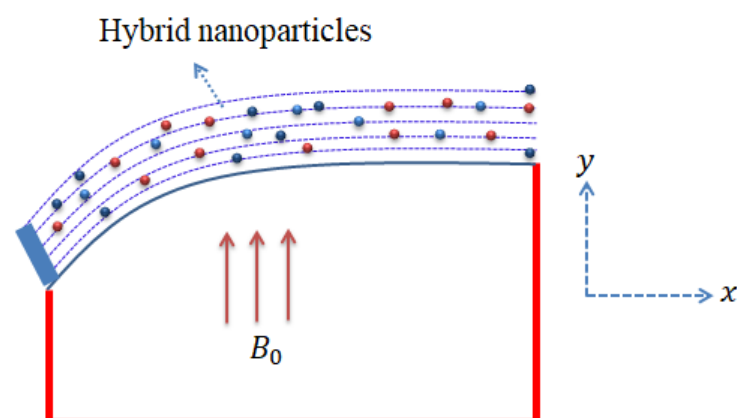


Figure 2. Geometrical sketch of flow problem.

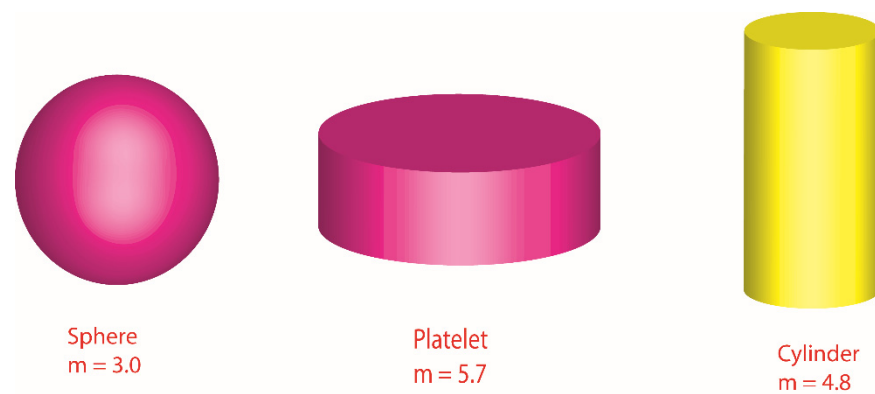


Figure 3. Illustration of various shapes related to nanoparticles.

The system of PDEs is formulated using the above assumptions, and non-linear PDEs are modeled as

$$\frac{\partial \tilde{U}}{\partial x} + \frac{\partial \tilde{V}}{\partial y} = 0, \quad (1)$$

$$\begin{aligned} \tilde{U} \frac{\partial \tilde{U}}{\partial x} + \tilde{V} \frac{\partial \tilde{V}}{\partial y} - \frac{\partial}{\partial x} \left[\left(xGY \left(\frac{m+1}{2} \right) \right) (T - T_\infty) \right] - \frac{\partial}{\partial x} \left[\left(G^* xY \left(\frac{m+1}{2} \right) \right) (C - C_\infty) \right] \\ = - \frac{(B_0)^2 \sigma_{hmf}}{\rho_{hmf}} \tilde{U} + \left(\nu_{hmf} + \frac{1}{c\alpha\rho_{hmf}} \right) \frac{\partial^2 \tilde{U}}{\partial y^2} - \frac{1}{2c^3\alpha\rho_{hmf}} \left(\frac{\partial \tilde{U}}{\partial y} \right)^2 \frac{\partial^2 \tilde{U}}{\partial y^2}, \end{aligned} \quad (2)$$

$$\tilde{U} \frac{\partial T}{\partial x} + \tilde{V} \frac{\partial T}{\partial y} = \frac{k_{hmf}}{(\rho C_p)_{hmf}} \frac{\partial^2 T}{\partial y^2} + \frac{(B_0)^2 \sigma_{hmf}}{(\rho C_p)_{hmf}} (\tilde{U})^2 + \frac{K_T D_{hmf}}{C_s (C_p)_f} \left(\frac{\partial^2 C}{\partial y^2} \right) + \frac{Q}{(\rho C_p)_{hmf}} (T - T_\infty), \quad (3)$$

$$\tilde{U} \frac{\partial C}{\partial x} + \tilde{V} \frac{\partial C}{\partial y} = D_{hmf} \left(\frac{\partial^2 C}{\partial y^2} \right) - k_1 (C - C_\infty) + \frac{K_T D_{hmf}}{T_m} \left(\frac{\partial^2 T}{\partial y^2} \right) - \exp \left(- \frac{En}{K_t} \right) \left(\frac{T}{T_\infty} \right)^n (k_r)^2 (C - C_\infty), \quad (4)$$

The following boundary conditions are excluded to determine the physical behavior of the current model:

$$\tilde{U} = a(y+x)^m, \tilde{V} = 0, T = T_w, C = C_w \text{ at } y = a^*(b+x)^{1-m/2}, \tilde{U} \rightarrow 0, C \rightarrow C_\infty, T \rightarrow T_\infty \text{ at } y \rightarrow \infty. \quad (5)$$

The variables are changed using the theory of no-slip, and the change in variables are

$$\begin{aligned} \psi = F \sqrt{\frac{a^2(x+b)^{m+1} \nu_f}{m+1}}, \tilde{U} = a(x+b)^m F_\zeta, \zeta = \sqrt{\frac{a(m+1)(x+b)^{m-1}}{2\nu_f}} \\ \tilde{V} = - \sqrt{\frac{a\nu_f(m+1)(x+b)^{m-1}}{2}} \left[F + \eta \left(\frac{m-1}{m+1} \right) F_\zeta \right], \Theta = \frac{T-T_\infty}{T_w-T_\infty}, \Phi = \frac{C-C_\infty}{C_w-C_\infty}. \end{aligned} \quad (6)$$

Transformers are used in Equations (2)–(6), and the nine modeled (ordinary differential equations) are

$$\begin{aligned} \left(1 + \epsilon(1-\phi_1)^{2.5}(1-\phi_2)^{2.5} \right) F_{\zeta\zeta\zeta} - \epsilon(1-\phi_2)^{2.5}(1-\phi_1)^{2.5} \delta^* (F_{\zeta\zeta})^2 F_{\zeta\zeta\zeta} \\ + A_1 \left(FF_{\zeta\zeta} - \frac{2m}{m+1} (F_\zeta)^2 \right) + A_1 GR\Theta + A_1 Re\Phi - \frac{\sigma_{hmf}}{\sigma_f} M^2 F_\zeta = 0, \end{aligned} \quad (7)$$

$$\Theta_{\zeta\zeta} + A_2 PrF\Theta_\zeta + A_3 PrECM^2 (F_\zeta)^2 + A_4 H_s \Theta + A_4 A_5 PrD_F \Phi_{\zeta\zeta} = 0, \quad (8)$$

$$\begin{aligned} \Phi_{\xi\xi} + \frac{Sc}{(1-\phi_2)^{2.5}(1-\phi_1)^{2.5}} F\Phi_\xi - \frac{K_c Sc}{(1-\phi_2)^{2.5}(1-\phi_1)^{2.5}} \Phi + ScSr\Theta_{\xi\xi} \\ - \frac{Sc}{(1-\phi_2)^{2.5}(1-\phi_1)^{2.5}} (1 + \delta\Theta)^n \Phi \Gamma \exp \left(- \frac{E}{1+\delta\Theta} \right) = 0. \end{aligned} \quad (9)$$

The dimensionless boundary conditions of Equations (7)–(9) are

$$\begin{aligned} F(0) &= \alpha_1 \left(\frac{1-m}{1+m} \right), F_\zeta(0) = 1, F_\zeta(\infty) = 0, \\ \Theta(0) &= 1, \Theta(\infty) = 0, \Phi(0) = 1, \Phi(\infty) = 0, \end{aligned} \quad (10)$$

$$F(\eta) = f(\eta) = F(\eta - \alpha_1), \Theta(\eta) = \Theta(\eta - \alpha_1) = \Theta(\eta), \Phi(\eta) = \Phi(\eta - \alpha_1) = \Phi(\eta). \quad (11)$$

Equation (11) is used in Equations (7)–(9), which gives

$$\begin{aligned} & \left(1 + \epsilon(1 - \phi_2)^{2.5}(1 - \phi_1)^{2.5} \right) f_{\zeta\zeta\zeta} - \epsilon(1 - \phi_2)^{2.5}(1 - \phi_1)^{2.5} (f_{\zeta\zeta})^2 f_{\zeta\zeta\zeta} \\ & + A_1 \left(f f_{\zeta\zeta} - \frac{2m}{m+1} (f_\zeta)^2 \right) + A_1 GR\theta + A_1 Re\varphi - \frac{\sigma_{hmf}}{\sigma_f} M^2 f_\zeta = 0, \end{aligned} \quad (12)$$

$$\theta_{\zeta\zeta} + A_2 Pr f \theta_\zeta + A_4 Pr ECM^2 (f_\zeta)^2 + A_4 H_s \theta + A_4 A_5 Pr D_F \varphi_{\zeta\zeta} = 0, \quad (13)$$

$$\begin{aligned} \varphi_{\zeta\zeta} + \frac{Sc}{(1-\phi_2)^{2.5}(1-\phi_1)^{2.5}} f \varphi_\zeta - \frac{K_c Sc}{(1-\phi_2)^{2.5}(1-\phi_1)^{2.5}} \varphi + Sc Sr \theta_{\zeta\zeta} \\ - \frac{Sc}{(1-\phi_2)^{2.5}(1-\phi_1)^{2.5}} (1 + \delta\theta)^n \Gamma \varphi \exp\left(-\frac{E}{1+\delta\theta}\right) = 0. \end{aligned} \quad (14)$$

The BCs of Equations (12)–(14) are constructed as

$$\begin{aligned} f(0) &= \alpha_1 \left(\frac{1-m}{1+m} \right), f_\zeta(0) = 1, f_\zeta(\infty) = 0, \\ \theta(0) &= 1, \theta(\infty) = 0, \varphi(0) = 1, \varphi(\infty) = 0. \end{aligned} \quad (15)$$

Here, the parameters related to nanoparticles and hybrid nanoparticles are

$$\begin{aligned} A_1 &= (1 - \phi_1)^{2.5}(1 - \phi_2)^{2.5} \left[(1 - \phi_2) \left\{ (1 - \phi_1) + \phi_1 \frac{\rho_{s1}}{\rho_f} \right\} \right] + \phi_2 \frac{\rho_{s2}}{\rho_f}, \\ A_2 &= A_4 \left[(1 - \phi_2) \left\{ (1 - \phi_1) + \phi_1 \frac{(\rho C_p)_{s1}}{(\rho C_p)_f} \right\} \right] + \phi_1 \frac{(\rho C_p)_{s2}}{(\rho C_p)_f}, A_4 = \frac{k_f}{k_{hmf}}, \end{aligned} \quad (16)$$

$$A_5 = (1 - \phi_1)^{2.5}(1 - \phi_2)^{2.5} \left[(1 - \phi_2) \left\{ (1 - \phi_1) + \phi_1 \frac{(\rho C_p)_{s1}}{(\rho C_p)_f} \right\} \right] + \phi_1 \frac{(\rho C_p)_{s2}}{(\rho C_p)_f}, \quad (17)$$

$$\frac{k_{hmf}}{k_{bf}} = \left\{ \frac{k_{s2} + (n-1)k_{bf} - (n-1)\phi_2(k_{bf} - k_{s2})}{k_{s2} + (n-1)k_{bf} - \phi_2(k_{bf} - k_{s2})} \right\}. \quad (18)$$

where the fluid parameter (ϵ), thermal Grashof (GR), bio-convection Rayleigh (Re), magnetic (M^2), Prandtl (Pr), Eckert (EC), Dufour (D_F), chemical reaction (K_c), Schmidt (Sc), Soret (Sr), activation energy (E) and temperature difference (δ) numbers are derived as

$$\epsilon = \frac{1}{\alpha \mu_f}, GR = \frac{Y(T_w - T_\infty)G}{a^2(b+x)^{2m-1}}, Re = \frac{Y(C_w - C_\infty)G}{a^2(b+x)^{2m-1}}, M^2 = \frac{2(B_0)^2 \sigma_f}{\rho_f(m+1)a(b+x)^{m-1}}, \quad (19)$$

$$Pr = \frac{\mu_f(C_p)_f}{k_f}, Ec = \frac{(b+x)^{2m}a}{(T_w - T_\infty)^2(C_p)_f}, Sc = \frac{\nu_f}{D_f}, \delta = \frac{T_w - T_\infty}{T_\infty}, E = \frac{En}{(x+b)T_\infty}, \quad (20)$$

$$K_c = \frac{2k_r}{(m+1)a(x+b)^{m-1}}, D_F = \frac{D_f(C_w - C_\infty)K_t}{\nu_f C_s (T_w - T_\infty)(C_p)_f}, Sr = \frac{K_t D_f (T_w - T_\infty)}{\nu_f T_m (C_w - C_\infty)}. \quad (21)$$

The present flow model is known as the pure fluid model for $\phi_1 = \phi_2 = 0$. Equation (2) is called the continuity equation, while Equation (3) is known as a momentum equation (in x -direction). The first two terms (on the LHS of Equation (3)) are inertial forces, and the last two terms (on the LHS of Equation (3)) are impacts related to heat energy and concentration due to gravitational force (acting downward on the parabolic surface). The first term (on

the RHS of Equation (3)) is known as a Lorentz force, whereas the last two terms (on the RHS of Equation (3)) occur due to the presence of Eyring–Powell fluid. Equation (4) shows the heat energy equation, and the first two terms (on the LHS of Equation (4)) appear due to convective heat transfer. The first term (on the RHS of Equation (4)) is Fourier’s law (of heat conduction), and the last three terms (on the RHS of Equation (4)) are Joule heating, Dufour effect and heat generation, respectively. Equation (5) is the concentration equation; the first two terms (on the LHS of Equation (5)) are the diffusion of mass species (through convection) while the last four terms (on the RHS of Equation (5)) are known as Fick’s law, the chemical reaction, the Soret effect and the activation energy, respectively. Thermal properties of hybrid nanoparticles and nanoparticles are mentioned in Table 1.

Table 1. Thermal properties of hybrid nanoparticles and nanoparticles in base fluid.

<i>Cu</i>	<i>C₂H₆O₂</i>	<i>Al₂O₃</i>
$\rho_{Cu} = 8933$	$\rho_{C_2H_6O_2} = 1113.5$	$\rho_{Al_2O_3} = 3970$
$(C_p)_{Cu} = 4179$	$(C_p)_{C_2H_6O_2} = 2430$	$(C_p)_{Al_2O_3} = 765$
$k_{Cu} = 0.613$	$k_{C_2H_6O_2} = 0.253$	$k_{TAl_2O_3} = 40$
$\sigma_{Cu} = 5.5 \times 10^{-6}$	$\sigma_{C_2H_6O_2} = 4.3 \times 10^{-5}$	$\sigma_{Al_2O_3} = 5.96 \times 10^7$

The surface force at the wall of the parabolic surface is modeled as

$$C_f = \frac{\tau_{at\ wall}}{\rho_{hnf} (a(b+x)^m)^2} \frac{(Ree)^{0.5} C_f}{\left(\frac{m+1}{2}\right)^{0.5}} = \frac{(1-\phi_2)^{-2.5}}{(1-\phi_1)^{2.5}} \left[(1+\epsilon) f_{\zeta\xi}(0) - \epsilon \delta^* (f_{\zeta\xi}(0))^3 \right] \quad (22)$$

The gradient temperature in the combination of hybrid nanoparticles and nanoparticles is

$$(Ree)^{0.5} Nu \left(\frac{m+1}{2} \right)^{-1/2} = A_4 \theta'(0). \quad (23)$$

The Sherwood number reflects the existence of activation energy, and is modeled as

$$(Ree)^{0.5} Sh \left(\frac{m+1}{2} \right)^{-1/2} = \frac{1}{(1-\phi_2)^{2.5} (1-\phi_1)^{2.5}} \phi'(0). \quad (24)$$

Here, the local Reynolds is known as $Ree = \frac{(b+x)^{m+1} a}{\nu_f}$.

3. Grid Independent Analysis and Numerical Approach

The numerical approach is adopted as a finite element scheme (FEM) to compute the solution of highly non-linear ODEs. The domain of the current model is broken into small segments called finite element schemes. FEM is used in electrical systems, solid mechanics, chemical processing and fluid-related problems, etc. The related steps of FEM are listed below.

Construction of residuals: The collection of all terms on one side provides the residuals. The present model (Equations (12)–(15)) is called the strong form, while this strong form is reduced to its weak form by integrating the non-linear terms. It is noticed that the order of ODEs is reduced by considering the term $f' = T$. The simplified residuals are

$$\int_{\eta_e}^{\eta_{e+1}} wh_1 [f' - T] d\eta = 0, \quad (25)$$

$$\int_{\eta_e}^{\eta_{e+1}} wh_2 \left[\theta_{\zeta\xi} + A_2 Pr f \theta_{\zeta} + A_4 Pr ECM^2 (T)^2 + A_4 H_s \theta + A_4 A_5 Pr D_F \varphi_{\zeta\xi} \right] d\eta = 0, \quad (26)$$

$$\int_{\eta_e}^{\eta_{e+1}} wh_3 \left[\varphi_{\zeta\xi} + \frac{Sc}{(1-\phi_2)^{2.5} (1-\phi_1)^{2.5}} f \varphi_{\zeta} - \frac{K_c Sc}{(1-\phi_2)^{2.5} (1-\phi_1)^{2.5}} \varphi + Sc Sr \theta_{\zeta\xi} - \frac{Sc}{(1-\phi_2)^{2.5} (1-\phi_1)^{2.5}} (1 + \delta \theta)^n \Gamma \varphi \exp \left(-\frac{E}{1 + \delta \theta} \right) \right] d\eta = 0. \quad (27)$$

Here $wh_l, l = 1, 3$ are the weight functions and ψ_i is the shape function.

Mesh-free investigation: The current model has a physical domain $[0, \infty]$, while it is clear that the computational domain is generated using the concept of the satisfaction of asymptotic BCs. $[0, 8]$ is considered the computational domain, where η_{max} is considered to be 8. The graphical views of the computational and physical domains, and the division of the physical domain into elements, are addressed by Figures 4 and 5.

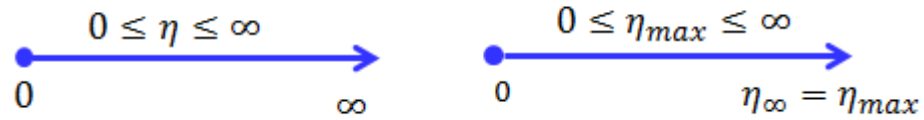


Figure 4. Geometrical view of physical domain and computational domain.

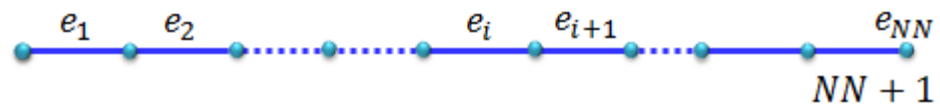


Figure 5. Division of physical domain into finite elements.

Assembly procedure: the Galerikin scheme is used to obtain the elements' stiffness matrix. The elements' stiffness matrix is developed using the assembly procedure. The elements' stiffness matrix is

$$K_{ij}^{11} = \int_{\eta_e}^{\eta_{e+1}} \psi_i \left(\frac{d\psi_j}{d\eta} \right) d\eta, K_{ij}^{12} = - \int_{\eta_e}^{\eta_{e+1}} \psi_i (\psi_j) d\eta, K_{ij}^{13} = 0, K_{ij}^{14} = 0, \quad (28)$$

$$K_{ij}^{22} = \int_{\eta_e}^{\eta_{e+1}} \left[\begin{array}{c} - (1 + \epsilon(1 - \phi_1)^{2.5} (1 - \phi_1)^{2.5}) \frac{d\psi_i}{d\eta} \frac{d\psi_j}{d\eta} \\ + \delta^* \epsilon(1 - \phi_1)^{2.5} (1 - \phi_1)^{2.5} (\bar{T}')^2 \frac{d\psi_i}{d\eta} \frac{d\psi_j}{d\eta} \\ + A_1 \left(\bar{f} \psi_i \frac{d\psi_j}{d\eta} - \frac{2m}{m+1} \bar{T} \psi_i \frac{d\psi_j}{d\eta} \right) - \frac{\sigma_{mf}}{\sigma_f} M^2 \psi_i \frac{d\psi_j}{d\eta} \end{array} \right] d\eta, K_{ij}^{21} = 0, \quad (29)$$

$$K_{ij}^{23} = \int_{\eta_e}^{\eta_{e+1}} A_1 GR \psi_i (\psi_j) d\eta, K_{ij}^{21} = 0, K_{ij}^{24} = \int_{\eta_e}^{\eta_{e+1}} A_1 Re \psi_i (\psi_j) d\eta, B_i^2 = 0, \quad (30)$$

$$K_{ij}^{33} = \int_{\eta_e}^{\eta_{e+1}} \left[- \frac{d\psi_j}{d\eta} \frac{d\psi_i}{d\eta} + A_2 Pr \bar{f} \frac{d\psi_j}{d\eta} \psi_i + A_4 H_s \psi_i \psi_j \right] d\eta, \quad (31)$$

$$K_{ij}^{34} = \int_{\eta_e}^{\eta_{e+1}} \left[- A_4 A_5 Pr D_F \frac{d\psi_i}{d\eta} \frac{d\psi_j}{d\eta} \right] d\eta, K_{ij}^{31} = 0, K_{ij}^{31} = 0, B_i^3 = 0, \quad (32)$$

$$K_{ij}^{44} = \int_{\eta_e}^{\eta_{e+1}} \left[\begin{array}{c} - \frac{d\psi_i}{d\eta} \frac{d\psi_j}{d\eta} + \frac{Sc}{(1 - \phi_2)^{2.5} (1 - \phi_1)^{2.5}} \bar{f} \psi_i \frac{d\psi_j}{d\eta} \\ - \frac{K_c Sc}{(1 - \phi_2)^{2.5} (1 - \phi_1)^{2.5}} \psi_i \psi_j \end{array} \right] d\eta, B_i^4 = 0, \quad (33)$$

$$K_{ij}^{43} = \int_{\eta_e}^{\eta_{e+1}} \left[\begin{array}{c} - Sc Sr \left(\frac{d\psi_j}{d\eta} \frac{d\psi_i}{d\eta} \right) - \frac{Sc}{(1 - \phi_2)^{2.5} (1 - \phi_1)^{2.5}} \times \\ \Gamma(1 + \delta\theta)^n \exp \left(- \frac{E}{1 + \delta\theta} \right) \psi_i \psi_j \end{array} \right] d\eta, \quad (34)$$

$$K_{ij}^{32} = \int_{\eta_e}^{\eta_{e+1}} A_4 Pr ECM^2 T \psi_j \psi_i d\eta, K_{ij}^{44} = 0, K_{ij}^{41} = 0. \quad (35)$$

Error investigation and simulation of equations: The system of ODEs is linearized using Picard linearization, considering the tolerance (10^{-8}). The convergence analysis is conducted as

$$Err = \left| \chi^i - \chi^{i-1} \right| \quad (36)$$

and the convergence criteria of the current model are defined as

$$Max \left| \chi^i - \chi^{i-1} \right| < 10^{-8}. \quad (37)$$

Study of grid independent: Maple 18 software is used to generate the code related to FEM. The solution of the current model is converged at 300 elements. The simulations of grid independent with 300 elements are given in Table 2.

Table 2. Mesh-free analysis of velocity, concentration and temperature at the middle of each of the 300 elements.

Number of Elements	$f_{\xi}(\frac{\eta_{\infty}}{2})$	$\theta(\frac{\eta_{\infty}}{2})$	$\varphi(\frac{\eta_{\infty}}{2})$
30	0.02563511179	0.5010430026	0.000002753767268
60	0.005590099064	0.4622252540	0.02471348366
90	0.005472897618	0.4564407494	0.02293467057
120	0.005415678507	0.4535558400	0.02208161164
150	0.005381789627	0.4518259302	0.02158116249
180	0.005359391320	0.4506744132	0.02125219796
210	0.005343470646	0.4498514616	0.02101947689
240	0.005331585746	0.4492371723	0.02084607618
270	0.005322299522	0.4487571006	0.02071193875
300	0.005314946586	0.4483716081	0.02060532127

4. Results and Discussion

This section contains graphical discussions of flow behavior, solute particles and thermal energy in the presence of the Dufour and Soret effects, including various shapes (cylinder, platelet and sphere) of nanoparticles. The flow of solute particles is affected by the presence of activation energy and chemical reactions, whereas the transfer of thermal energy occurs in the presence of heat generation phenomena. The effects of bio-convection and magnetic fields are also imposed upon Eyring–Powel liquid containing hybrid nanoparticles and nanoparticles. The finite element method is used to determine the effects of various parameters on solute particles' temperature and velocity profiles. The outcomes are captured below:

4.1. Comparative Analysis of Flow Behavior in Hybrid Nanoparticles and Nanoparticles

A comparative analysis between hybrid nanoparticles and nanoparticles is carried out in the flow behavior of Eyring–Powel liquid, considering cylinder, platelet and sphere nanoparticles. Such analysis is simulated with the inclusion of various physical parameters, as considered by Figures 6–10. Hybrid nanoparticles are called Cu/Al_2O_3 and nanofluid is taken as Cu in the base fluid (ethylene glycol). Moreover, solid lines are plotted for Cu/Al_2O_3 and dotted lines plot the influence of Cu . The effect of ϵ on the flow of fluid particles over a stretched surface is visualized by Figure 6. The effect of an increment in fluid speed on hybrid nanoparticles and nanoparticles is investigated using the large values of ϵ . The speed of hybrid nanoparticles becomes higher, and the speed of nanoparticles does not. The thickness of the momentum boundary layer becomes higher via an enlargement of the fluid parameter. Physically, the parameter related to ϵ is affected by the presence of Darcy's porous medium in relation to fluid particles. The retardation force impacts fluid particles due to the presence of Darcy's porous medium. MBL (momentum boundary layer thickness) is also managed with the help of ϵ . Figure 7 illustrates the role of the flow in nanoparticles and Cu/Al_2O_3 versus the change in the power law index number (m). The parameter related to m is observed in the flow model due to the parabolic surface. m acts as a drag force in the flow of Cu/Al_2O_3 and Cu . The higher values of m bring about a reduction in the speed of flow over a heated parabolic surface. In Figure 7, the speed of flow attains the maximum speed in the hybrid nanoparticles rather than the nanoparticles in ethylene glycol. The thickness of boundary layers becomes reduced by applying large values of m . The parameter related to the power law number (m) is affected by the transformations in the current model. Moreover, the thickness of the boundary layer is reduced with higher values of the power law number. Hence, the fluid becomes thick with positive values of the power law number. The effect of Re (bio-convection Rayleigh) on

the speed of the fluid particles is measured by Figure 8. It is noticed that the motion of fluid particles becomes slow due to the enlargement of Re . The flow of hybrid nanoparticles and nanoparticles is higher than the flow of Cu -nanoparticles. The thicknesses of momentum boundary layers are also reduced with positive values of Re . Figure 9 captures the flow behavior in nanoparticles and hybrid nanoparticles with changes in GR. This parameter is very useful to attain the maximum flow of fluid particles over a parabolic surface. An enhancement in flow occurs due to the higher values of the Grashof number, based on the volumetric (thermal expansion) coefficient. Hence, the Grashof number causes an increment in flow behavior, since the thermal Grashof parameter (GR) is based on coefficient (volumetric thermal) expansion. Therefore, the thermal Grashof parameter (GR) generates an enhancement in fluid motion. Moreover, the thickness of the momentum boundary layer in hybrid nanoparticles is greater than the MBLT of nanoparticles. Hence, hybrid nanoparticles generate the maximum flow in fluid nanoparticles.

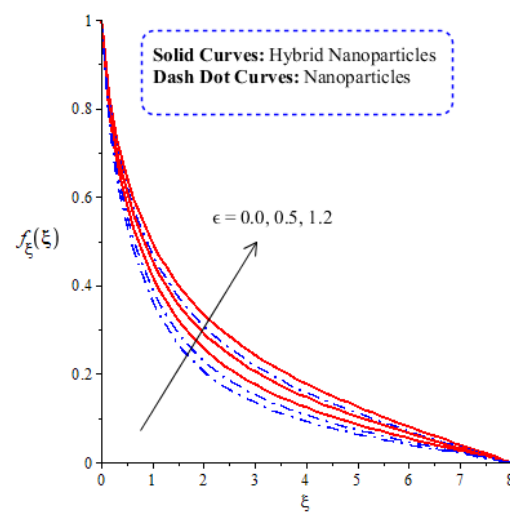


Figure 6. Comparative analysis of velocity in hybrid nanoparticles and nanoparticles versus change in ϵ .

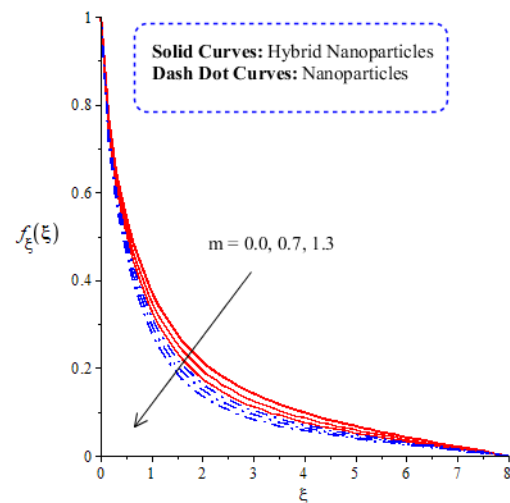


Figure 7. Comparative analysis of velocity in hybrid nanoparticles and nanoparticles versus change in m .

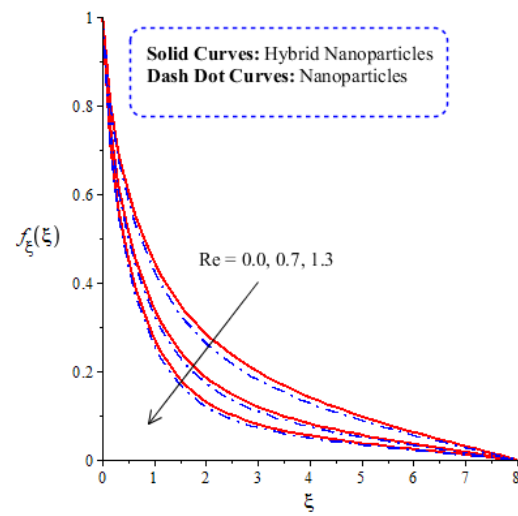


Figure 8. Comparative analysis of velocity in hybrid nanoparticles and nanoparticles versus change in Re .

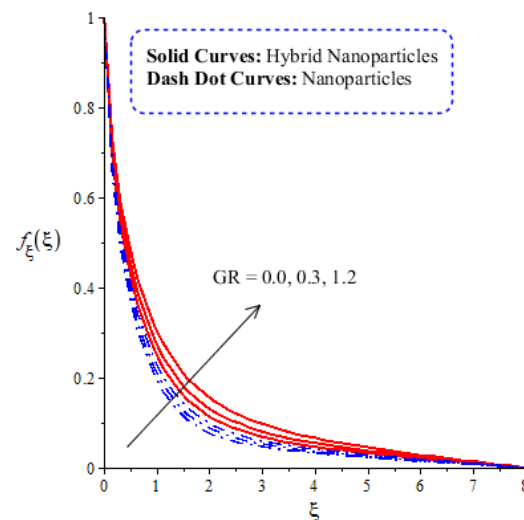


Figure 9. Comparative analysis of velocity in hybrid nanoparticles and nanoparticles versus change in GR .

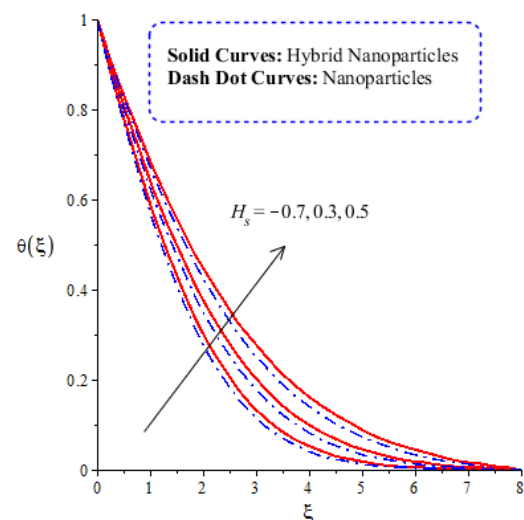


Figure 10. Comparative analysis of thermal energy in hybrid nanoparticles and nanoparticles versus change in H_s .

4.2. Comparative Analysis of Thermal Energy in Hybrid Nanoparticles and Nanoparticles

The variation in thermal energy is assessed versus the change in the Dufour, heat generation, Eckert and magnetic numbers. The influences of the Dufour, heat generation, Eckert and magnetic numbers on the transfer of heat energy are captured by Figures 10–13. The effect of the heat generation number on the transfer of heat energy is displayed by Figure 10. The maximum heat energy is attained via the enlargement of H_s . It is estimated that negative values relate to the absorption of thermal energy, while positive values of H_s relate to the generation of thermal energy. The graphical representation illustrates strong absorption via the higher negative values of H_s . The term of H_s in the dimensionless energy equation is affected by the appearance of heat generation. The maximum heat energy is generated by hybrid nanoparticles (Cu/Al_2O_3) rather than Cu -nanoparticles. Hence, H_s is the best physical parameter in view of attaining the maximum amount of heat energy. The dual role H_s in heat energy relates to the positive and negative values of H_s . Physically, H_s is generated in the energy equation because of the external heat source. As such, thermal aspects can be adjusted according to the values of H_s . The comparative analysis in view of thermal energy, taking into account the impact of D_f , is plotted by Figure 11. The increasing effect of D_f on the transfer of thermal energy is visualized by Figure 11. The Soret and Dufour effects are inserted into the mass diffusion and heat energy equations. The fluid particles become more heated following the involvement of D_f . Hybrid nanoparticles are more able to attain the maximum amount of heat energy than nanoparticles. The effect of the Dufour number (D_f) in the heat energy equation (Dimensionless) occurs because of the first law of thermodynamics. This law states that the transport of heat energy is due to the concentration gradient. The fluid particles carry more heat energy at the surface due to the diffusing of the nanoparticles into fluid. Figure 12 demonstrates the effects of EC on thermal energy, as is further captured by Figure 13. EC has an effect due to the role of viscous dissipation in the dimensionless energy equation. Physically, the direct relation between viscous dissipation and EC is plain. The large values of EC relate to the maximum viscous dissipation. Hence, more kinetic energy is produced in fluid particles, considering the impacts of nanoparticles and hybrid nanoparticles. Moreover, the inclusion of hybrid nanoparticles helps attain more heat energy than nanoparticles. The Eckert number (EC) is also known as the work done by fluid particles. Positive values of EC motivate the particles to carry more heat energy. So, the temperature of fluid particles is increased by viscous dissipation. The variation in the effect of the magnetic number on the transfer of heat energy is illustrated by Figure 13. An increment in thermal energy is manifested by large values of the magnetic number. Physically, the magnetic number in the dimensionless energy equation is generated by the role of the Joule heating phenomenon. The Joule heating phenomenon brings about increments in thermal energy via higher values of magnetic number. Joule heating is defined as the transformation of electrical energy into heat energy. The fluid particles become heated due to the dissipation of heat energy.

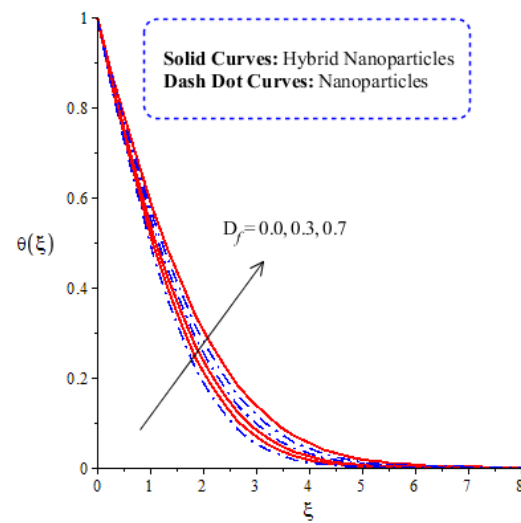


Figure 11. Comparative analysis of thermal energy in hybrid nanoparticles and nanoparticles with changes in D_f .

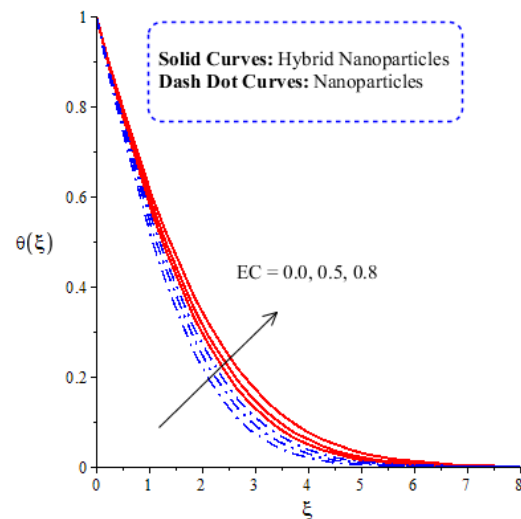


Figure 12. Comparative analysis of thermal energy in hybrid nanoparticles and nanoparticles with changes in EC .

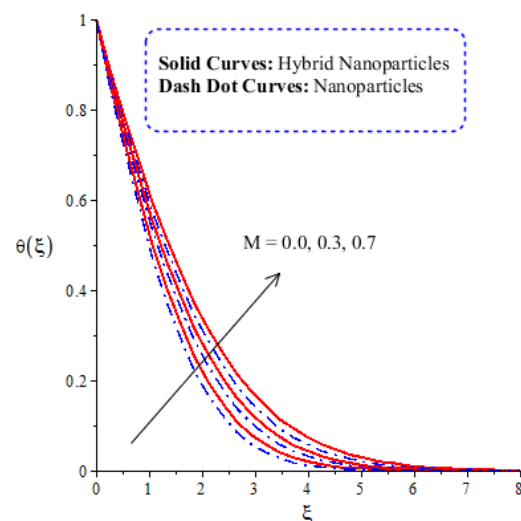


Figure 13. Comparative analysis of thermal energy in hybrid nanoparticles and nanoparticles with changes in M .

4.3. Comparative Analysis of Solute Particles in Hybrid Nanoparticles and Nanoparticles

Figures 14–17 show the comparative analysis of solute particles in hybrid nanoparticles and nanoparticles with variations in various parameters Sc , E , Sr and K_c . The graph of diffusion mass species versus Sc is plotted in Figure 14. A reduction occurs in solute particles with the variation in Sc . According to the definition of Sc , solute particles slow down following a reduction in mass diffusion. From another point of view, hybrid nanoparticles are more concentrated in solute particles compared to nanoparticles affected by Sc . The thicknesses of concentration layers are reduced via the enlargement of Sc . The impact of activation energy (E) on solute particles can be observed in Figure 15. It is clear that a modification of the Arrhenius function brings about an enlargement in activation energy. The diffusion of solute particles is enhanced because of the activation energy. Activation energy provides more heat energy to fluid particles. The process of diffusion becomes fast. Further, the thickness of the boundary layer is increased with larger values of E . Figure 16 illustrates the impact of Sr on the chemical species, including the evolution of hybrid nanoparticles and nanoparticles. Sr is a coefficient term based on temperature gradient. The diffusion of solute particles increases with the temperature gradient. The physical parameter related to Sr is related to the concept of the Soret number. The Soret number increases solute particles. There are less chemical species of nanoparticles (Cu) than there are of hybrid nanoparticles (Cu/Al_2O_3). In this figure, CBLT also increases with respect to Sr . The effect of concentration on the chemical reaction (K_c) is visualized by Figure 17. Positive values of K_c result in a generative chemical reaction, while the tendency of chemical species to transport is reduced. In this investigation, the chemical reaction related to the first order is discussed in the equation (concentration). Further, destructive chemical reactions occur with positive values of the chemical reaction number. $K_c = 0$ occurs when no reaction happens. This kind of reaction is seen as more significant than the destructive chemical reaction. The chemical species of hybrid nanoparticles are greater in number than the chemical species generated by nanoparticles.

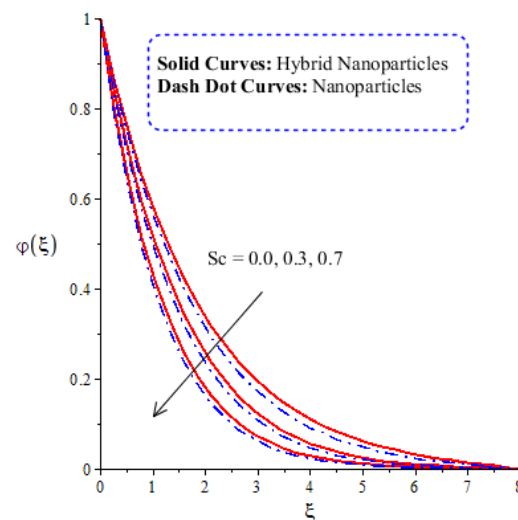


Figure 14. Comparative analysis of concentration in hybrid nanoparticles and nanoparticles with changes in Sc .

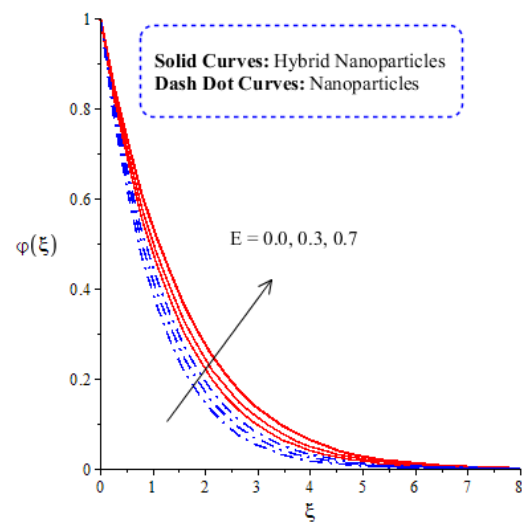


Figure 15. Comparative analysis of concentration in hybrid nanoparticles and nanoparticles with changes in E .

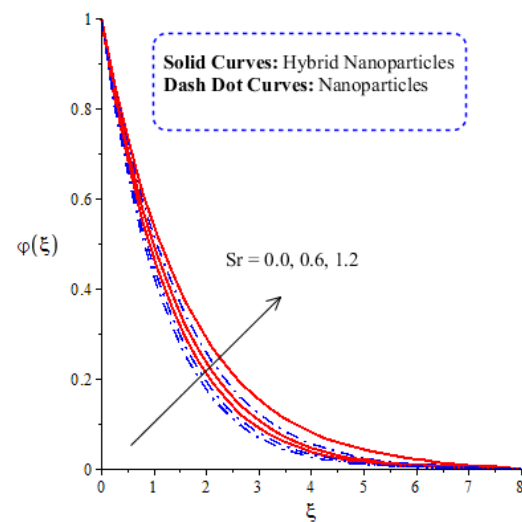


Figure 16. Comparative analysis of concentration in hybrid nanoparticles and nanoparticles with changes in Sr .

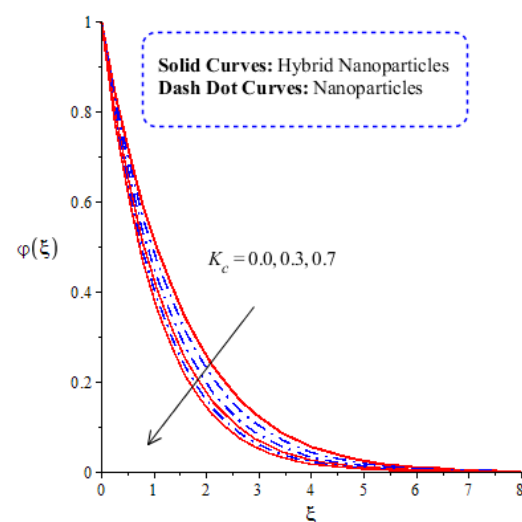


Figure 17. Comparative analysis of concentration in hybrid nanoparticles and nanoparticles with changes in K_c .

4.4. Comparative Simulations of Gradient Temperature, Surface Force and Rate of Solute Particles in Hybrid Nanoparticles and Nanoparticles

The gradient velocity, Sherwood number and temperature gradient are measured against the changes in ϵ , M , H_s , D_f and Sc in hybrid nanoparticles and nano-structures. Table 3 shows a comparative analysis between hybrid nano-structures and nano-structures. The velocity gradient is enhanced with the variation in ϵ , M and D_f , whereas the velocity gradient decreases with the enhancement in H_s and Sc . It is important to mention that the flow of hybrid nanoparticles is significantly increased as compared to nanoparticles in ethylene glycol. The temperature gradient becomes greater with larger values of ϵ , M and Sc . Hence, the roles of M and Sc in obtaining the maximum production of heat energy are considered significant. However, the rate of heat energy production is decreased with higher values of H_s and Sc . Table 3 shows that hybrid nanoparticles are very useful for obtaining the maximum production of heat energy, as compared to nanoparticles. Rate mass diffusion has a similar impact as gradient temperature. In this case, hybrid nanoparticles are much more significant in obtaining the maximum rate of mass diffusion as compared to nanoparticles.

Table 3. Numerical values of $(Re\epsilon)^{0.5}Nu\left(\frac{m+1}{2}\right)^{-1/2}$ and $-(Re\epsilon)^{0.5}Sh\left(\frac{m+1}{2}\right)^{-1/2}$ versus ϵ , M , H_s , D_f and Sc in nanoparticles and hybrid nanoparticles.

		Nanoparticles (Cu)			Hybrid Nanoparticles (Cu/Al ₂ O ₃)		
		Surface Force	Nusselt Number	Sherwood Number	Surface Force	Nusselt Number	Sherwood Number
ϵ	0.2	1.924813	1.565118	0.1384307	2.945961	2.565701	2.1399317
	0.5	0.221389	1.754730	0.5383389	2.549771	2.755495	2.3398409
	0.7	0.161556	1.940713	0.8382172	2.451139	2.946134	2.7397592
M	0.0	1.512261	0.7328196	0.1368876	2.998115	2.533346	2.1396489
	0.5	1.946357	1.530040	0.1381261	2.972760	2.731219	2.3396312
	0.8	1.988206	1.725651	0.1390913	2.982020	2.926860	2.7395964
H_s	−1.3	1.414523	1.459182	0.1383186	2.063254	2.460611	2.1398258
	0.3	1.262850	1.235944	0.1269818	2.074621	2.481310	2.1598612
	0.5	1.185876	1.501063	0.7124085	2.077686	2.499332	2.3398757
D_f	0.0	1.908737	1.187635	0.4380280	2.077922	2.443122	3.1398757
	0.3	1.908929	1.195251	0.2380280	2.078114	2.346892	3.1098757
	0.7	1.909124	1.299087	0.1380280	2.079462	2.152565	3.0398760
Sc	0.0	1.069600	1.512535	0.2237168	2.117654	2.511689	3.2259912
	1.3	1.129306	1.797270	0.3764354	2.178452	2.496630	3.2791166
	2.5	1.153055	1.985977	0.5326884	2.218099	2.488496	3.0189080

5. Prime Consequences of Current Model

Assessments of the thermal energy and chemical species in the presence of heat generation, and Dufour and Soret effects, are addressed in Eyring–Powel liquid with nanoparticles (cylinder, platelet and sphere) and hybrid nano-structures over a heated parabolic surface. The roles of activation energy and chemical reactions are included in the mass diffusion equation. The term related to bio-convection is also incorporated into the flow phenomenon. The numerical approach (FEM) is adopted to simulate numerical results of the current model. The prime consequences of the present study are listed below:

Three hundred elements are required for the convergence analysis of the current flow phenomenon;

Hybrid nanoparticles (Cu/Al₂O₃) are very significant in the context of solute particles, the flow of fluid particles and thermal energy, as compared to nanoparticles (Cu);

A greater acceleration of fluid particles is captured by the fluid parameter and the bio-convection Rayleigh number, whereas declinations in flow are indicated by enlargements in power law index and thermal Grashof number;

The performance of thermal energy is maximized by inserting the highest values of the magnetic, Dufour, heat generation and Eckert numbers;

The diffusion of solute particles increases due to increments in the values of activation energy and Soret number. However, the diffusion of solute particles decreases when using higher values of Schmidt and chemical reaction numbers;

Hybrid nanoparticles are very significant to obtaining the maximum rate of flow, heat energy and concentration, compared to nanoparticles;

Divergent velocity is enhanced by using large values of fluid number, magnetic number and Schmidt number, but reductions are seen in divergent velocity with changes in the heat generation and Dufour numbers;

The temperature gradient increases with positive values of the fluid number, magnetic number and Schmidt number, while the gradient temperature decreases with changes in the heat generation and Dufour numbers. The same trend is noticed in the concentration gradient.

Author Contributions: Conceptualization, M.S. and U.N.; methodology, U.N.; software, U.N.; validation, M.S., M.M.S. and J.-R.L.; formal analysis, Y.-M.C.; investigation, M.M.S.; resources, M.S.; data curation, U.N.; writing—original draft preparation, M.S. and U.N.; writing—review and editing, U.N. and Y.-M.C.; visualization, J.-R.L.; supervision, M.S.; project administration, M.S. All authors have read and agreed to the published version of the manuscript.

Funding: This research received no external funding.

Institutional Review Board Statement: Not applicable.

Informed Consent Statement: Not applicable.

Data Availability Statement: The data used to support this study are included in the manuscript.

Conflicts of Interest: The authors declare that they have no conflicts of interest.

Nomenclature

Symbols	Used for	Symbols	Used for
\tilde{U}, \tilde{V}	Velocity components (m/s)	x, y	Space coordinates
G	Gravitational force (N)	$Wh_i, i = 1, 3$	Weight functions
m	Power law index number	T, T_∞	Temperature and ambient temperature
C, C_∞	Concentration and ambient concentration (Kg m^{-3})	B_0	Magnetic induction
k	Thermal conductivity (W m^{-1})	K_T	Thermal diffusion
D	Mass diffusion (m^2s^{-1})	C_s	Concentration susceptibility
C_p	Specific heat capacitance ($\text{J Kg}^{-1}\text{K}$)	Q	Heat generation
k_1	Chemical reaction (s^{-1})	T_m	Fluid mean temperature
E	Activation energy ($\text{J Kg}^{-1}\text{K}$)	k_t	
a, b	Constants	F	Dimensionless velocity
GR	Thermal Grashof	Re	Bio-convection Rayleigh
M^2	Magnetic field	Pr	Prandtl number
Ec	Eckert number	H_s	Heat generation number
Hnf, bf	Hybrid nanofluid	D_f	Dufour number
Sc	Schmidt number	Sr	Soret number
K_c	Chemical reaction number	Nu	Nusselt number
Sh	Sherwood number	Ree	Reynolds number
m^*	Size number of nanoparticles	C_f	Skin friction coefficient
Cu, Al_2O_3	Copper and aluminum oxide	$C_2H_6O_2$	Ethylene glycol

Greek Symbols

σ	Electrically conductivity (S.m^{-1})	γ	Volumetric coefficients
ρ	Fluid density (Kg.m^{-3})	∞	Infinite number
ψ	Stream function	Θ, θ	Dimensionless temperature
φ, Φ	Dimensionless concentration	ϕ_1, ϕ_2, ϕ	Volume fractions
ξ	Independent variable	ϵ	Fluid number
τ	Shear stress (N.m^{-2})	e	Euler number
δ	Temperature difference (K)	δ^*	Fluid number

References

- Islam, S.; Shah, A.; Zhou, C.Y.; Ali, I. Homotopy perturbation analysis of slider bearing with Powell–Eyring fluid. *Z. Für Angew. Math. Und Phys.* **2009**, *60*, 1178–1193. [[CrossRef](#)]
- Patel, M.; Timol, M.G. Numerical treatment of Powell–Eyring fluid flow using method of satisfaction of asymptotic boundary conditions (MSABC). *Appl. Numer. Math.* **2009**, *59*, 2584–2592. [[CrossRef](#)]
- Khan, N.A.; Aziz, S.; Khan, N.A. MHD flow of Powell–Eyring fluid over a rotating disk. *J. Taiwan Inst. Chem. Eng.* **2014**, *45*, 2859–2867. [[CrossRef](#)]
- Hayat, T.; Makhdoom, S.; Awais, M.; Saleem, S.; Rashidi, M.M. Axisymmetric Powell-Eyring fluid flow with convective boundary condition: Optimal analysis. *Appl. Math. Mech.* **2016**, *37*, 919–928. [[CrossRef](#)]
- Krishna, P.M.; Sandeep, N.; Reddy, J.R.; Sugunamma, V. Dual solutions for unsteady flow of Powell-Eyring fluid past an inclined stretching sheet. *J. Nav. Archit. Mar. Eng.* **2016**, *13*, 89–99. [[CrossRef](#)]
- Kumar, D.; Ramesh, K.; Chandok, S. Mathematical modeling and simulation for the flow of magneto-Powell-Eyring fluid in an annulus with concentric rotating cylinders. *Chin. J. Phys.* **2020**, *65*, 187–197. [[CrossRef](#)]
- Abdelsalam, S.I.; Sohail, M. Numerical approach of variable thermophysical features of dissipated viscous nanofluid comprising gyrotactic micro-organisms. *Pramana J. Phys.* **2020**, *94*, 1–12. [[CrossRef](#)]
- Sohail, M.; Naz, R. Modified heat and mass transmission models in the magnetohydrodynamic flow of Sutterby nanofluid in stretching cylinder. *Phys. A Stat. Mech. Appl.* **2020**, *549*, 124088. [[CrossRef](#)]
- Qi, W.H.; Wang, M.P.; Liu, Q.H. Shape factor of nonspherical nanoparticles. *J. Mater. Sci.* **2005**, *40*, 2737–2739. [[CrossRef](#)]
- Maraj, E.N.; Iqbal, Z.; Azhar, E.; Mehmood, Z. A comprehensive shape factor analysis using transportation of $\text{MoS}_2\text{-SiO}_2/\text{H}_2\text{O}$ inside an isothermal semi vertical inverted cone with porous boundary. *Results Phys.* **2018**, *8*, 633–641. [[CrossRef](#)]
- Iqbal, Z.; Maraj, E.N.; Azhar, E.; Mehmood, Z. A novel development of hybrid ($\text{MoS}_2\text{-SiO}_2/\text{H}_2\text{O}$) nanofluidic curvilinear transport and consequences for effectiveness of shape factors. *J. Taiwan Inst. Chem. Eng.* **2017**, *81*, 150–158. [[CrossRef](#)]
- Khanafer, K.; Vafai, K. A critical synthesis of thermophysical characteristics of nanofluids. *Int. J. Heat Mass Transf.* **2011**, *54*, 4410–4428. [[CrossRef](#)]
- Saba, F.; Ahmed, N.; Hussain, S.; Khan, U.; Mohyud-Din, S.T.; Darus, M. Thermal analysis of nanofluid flow over a curved stretching surface suspended by carbon nanotubes with internal heat generation. *Appl. Sci.* **2018**, *8*, 395. [[CrossRef](#)]
- Qasim, M.; Khan, Z.H.; Lopez, R.J.; Khan, W.A. Heat and mass transfer in nanofluid thin film over an unsteady stretching sheet using Buongiorno's model. *Eur. Phys. J. Plus* **2016**, *131*, 1–11. [[CrossRef](#)]
- Awais, M.; Hayat, T.; Ali, A.; Irum, S. Velocity, thermal and concentration slip effects on a magneto-hydrodynamic nanofluid flow. *Alex. Eng. J.* **2016**, *55*, 2107–2114. [[CrossRef](#)]
- Alharbi, S.O.; Nawaz, M.; Nazir, U. Thermal analysis for hybrid nanofluid past a cylinder exposed to magnetic field. *AIP Adv.* **2019**, *9*, 115022. [[CrossRef](#)]
- Mourad, A.; Aissa, A.; Mebarek-Oudina, F.; Jamshed, W.; Ahmed, W.; Ali, H.M.; Rashad, A.M. Galerkin finite element analysis of thermal aspects of $\text{Fe}_3\text{O}_4\text{-MWCNT}/\text{water}$ hybrid nanofluid filled in wavy enclosure with uniform magnetic field effect. *Int. Commun. Heat Mass Transf.* **2021**, *126*, 105461. [[CrossRef](#)]
- Nazir, U.; Nawaz, M.; Alqarni, M.M.; Saleem, S. Finite element study of flow of partially ionized fluid containing nanoparticles. *Arab. J. Sci. Eng.* **2019**, *44*, 10257–10268. [[CrossRef](#)]
- Rasool, G.; Wakif, A. Numerical spectral examination of EMHD mixed convective flow of second-grade nanofluid towards a vertical Riga plate using an advanced version of the revised Buongiorno's nanofluid model. *J. Therm. Anal. Calorim.* **2021**, *143*, 2379–2393. [[CrossRef](#)]